Earth and Planetary Science Letters 478 (2017) 132–142

Contents lists available at ScienceDirect

Earth and Planetary Science Letters

www.elsevier.com/locate/epsl

The kinematic evolution of the Macquarie Plate: A case study for the fragmentation of oceanic lithosphere

Hakkyum Choi [a,b], Seung-Sep Kim [b,*], Jérôme Dyment [c], Roi Granot [d], Sung-Hyun Park [a], Jong Kuk Hong [a]

[a] Korea Polar Research Institute, Incheon 21990, South Korea
[b] Department of Astronomy, Space Science and Geology, Chungnam National University, Daejeon 34134, South Korea
[c] Institut de Physique du Globe de Paris, CNRS UMR 7154, Sorbonne Paris Cité, Université Paris Diderot, Paris 75005, France
[d] Department of Geological and Environmental Sciences, Ben-Gurion University of the Negev, Beer-Sheva 84105, Israel

ARTICLE INFO

Article history:
Received 27 April 2017
Received in revised form 23 August 2017
Accepted 25 August 2017
Available online 19 September 2017
Editor: P. Shearer

Keywords:
marine magnetics
tectonics
plate reconstruction
Macquarie Plate

ABSTRACT

The tectonic evolution of the Southeast Indian Ridge (SEIR), and in particular of its easternmost edge, has not been constrained by high-resolution shipboard data and therefore the kinematic details of its behavior are uncertain. Using new shipboard magnetic data obtained by R/VIB *Araon* and M/V *L'Astrolabe* along the easternmost SEIR and available archived magnetic data, we estimated the finite rotation parameters of the Macquarie–Antarctic and Australian–Antarctic motions for eight anomalies (1o, 2, 2Ay, 2Ao, 3y, 3o, 3Ay, and 3Ao). These new finite rotations indicate that the Macquarie Plate since its creation ∼6.24 million years ago behaved as an independent and rigid plate, confirming previous estimates. The change in the Australian–Antarctic spreading direction from N–S to NW–SE appears to coincide with the formation of the Macquarie Plate at ∼6.24 Ma. Analysis of the estimated plate motions indicates that the initiation and growth stages of the Macquarie Plate resemble the kinematic evolution of other microplates and continental breakup, whereby a rapid acceleration in angular velocity took place after its initial formation, followed by a slow decay, suggesting that a decrease in the resistive strength force might have played a significant role in the kinematic evolution of the microplate. The motions of the Macquarie Plate during its growth stages may have been further enhanced by the increased subducting rates along the Hjort Trench, while the Macquarie Plate has exhibited constant growth by seafloor spreading.

1. Introduction

The south-easternmost corner of the Australian Plate was shaped by complex tectonic processes, including the fragmentation and formation of the Macquarie Plate (Fig. 1) (Cande and Stock, 2004a; DeMets et al., 1988). The major evidence for its formation some 6 Myr ago derives from inconsistencies between the rotation parameters describing the Australia–Antarctica relative motion across the easternmost Southeast Indian Ridge (SEIR), east of the George V Fracture Zone (FZ), compared with those calculated for the rest of the SEIR (Cande and Stock, 2004a). In particular, Cande and Stock (2004a) tested the fit of conjugate magnetic anomalies and fracture zones east of the George V FZ, and found that the Australian–Antarctic rotation produces growing, clockwise misfits on the Australian Plate, suggesting that the Macquarie Plate has moved ∼30 km east with respect to the Australian Plate. They concluded that the Macquarie Plate has remained a rigid and independent plate since 6 Ma. The formation of the Macquarie Plate might have resulted from a change in the direction of relative motion between the Australian and Pacific plates, which led to the subduction of young and buoyant oceanic crust into the Hjort Trench (Cande and Stock, 2004a; Hayes et al., 2009).

To reconstruct the tectonic history of the Macquarie Plate, it is crucial to gather shipboard geophysical data along the eastern SEIR, where few data currently exist (e.g., Seton et al., 2014). In this study, we first estimate rotation parameters for eight anomalies (1o, 2, 2Ay, 2Ao, 3y, 3o, 3Ay, and 3Ao, where 'y' represents the 'young end' of the normal polarity interval and 'o' the 'old end') identified across the eastern SEIR, using newly acquired shipboard magnetic data between 148°E and 166°E (red lines in Fig. 1). These results constrain the motion between the Macquarie–Antarctic plates for the last 7 Myr and reveal that segment KR1 (east of Balleny FZ, following the segment numbering of Crowley et al. (2015)) of the SEIR (Fig. 1) exhibits a major change in plate motion at ∼6.24 Ma, coinciding with the formation of

* Corresponding author.
E-mail address: seungsep@cnu.ac.kr (S.-S. Kim).

http://dx.doi.org/10.1016/j.epsl.2017.08.035

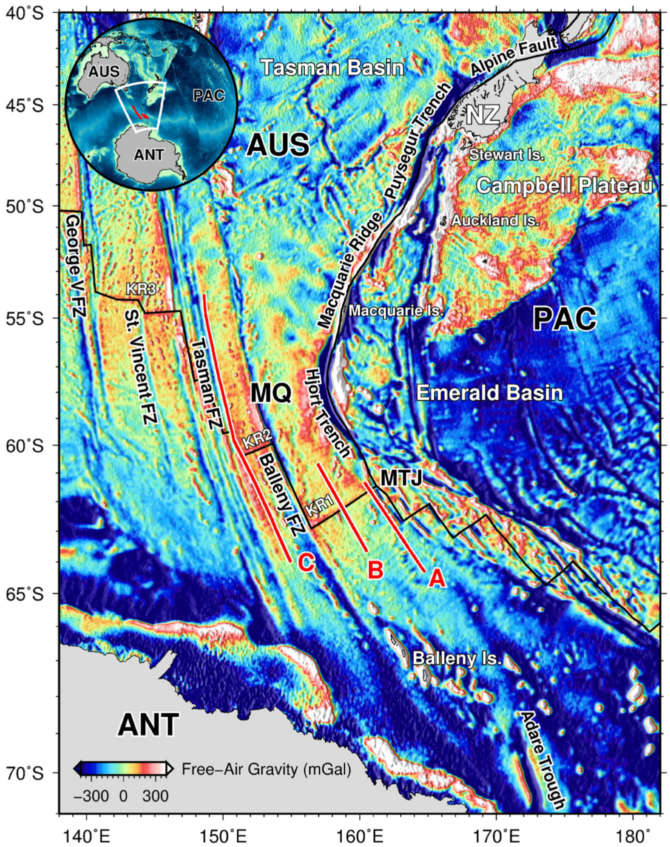

Fig. 1. Major tectonic features near the Southeast Indian Ridge (SEIR) and Macquarie Plate. New shipboard magnetic data were acquired along the red lines. The inset map provides a global perspective of the study region. PAC = Pacific Plate; AUS = Australian Plate; ANT = Antarctic Plate; NZ = New Zealand. The background map is the free-air gravity anomaly field (Sandwell et al., 2014). (For interpretation of the references to color in this figure legend, the reader is referred to the web version of this article.)

the Macquarie Plate. To investigate the Australian–Macquarie and Macquarie–Pacific plate motions, we also compute the Australian–Antarctic rotations (along the SEIR, west of ∼140°E) for the same eight anomalies. These new rotation parameters for the Australian–Macquarie–Antarctic plate motions enable us to better understand the formation and kinematic evolution of the Macquarie Plate.

2. Magnetic anomalies across the eastern SEIR

We conducted a series of interdisciplinary surveys between 2011 and 2015, over the eastern SEIR using the R/VIB *Araon*, collecting geological, geochemical, geophysical, hydrothermal, and biological data (Hahm et al., 2015). To constrain the tectonic history of the Macquarie Plate, two 400 km-long sea surface total field magnetic profiles (Lines A and B in Fig. 1) were obtained across segment KR1 in 2015. Each survey line was planned to gather at least 10 Myr of seafloor spreading records. For segment KR2 (west of the Balleny FZ), we acquired the magnetic data (Line C in Fig. 1) as part of the TACT (Tasmania–Adelie land Corridor Transect) program, using the M/V *L'Astrolabe* during the austral summer of 2012.

We reduced the magnetic data to anomalies using the International Geomagnetic Reference Field (IGRF) model 12 (Thébault et al., 2015). Then, we identified geomagnetic reversals by constructing forward magnetic models (Mendel et al., 2005), and estimated spreading parameters for the surveyed ridge segments (Fig. 2; see the detailed model parameters in Table S1 of the supplementary material). Following Cande and Stock (2004a) and Croon et al. (2008), who investigated the SEIR and the Pacific–Antarctic Ridge east of the study area, respectively, we adopted the geomagnetic polarity time scale of Cande and Kent (1995), except for C3Ay and C3Ao for which we used the updated ages of Krijgsman et al. (1999).

Fig. 2 shows the geomagnetic reversals identified from the observed marine magnetic data. Line A lies mostly on the southern flank of segment KR1 (Fig. 2a) (i.e., the Antarctic Plate), next to the Macquarie Triple Junction (MTJ) of the Australian–Antarctic–Pacific plates (Fig. 1). The identified magnetic anomalies along Line A show the spreading records from the ridge axis to anomaly 5o (10.95 Ma) southward, and to anomaly 1o (0.78 Ma) northward. The average full-spreading rates are estimated to be 63∼65 mm/yr (Table S1). Interestingly, a doubled crust, requiring a northward ridge-jump, is identified at ∼6.24 Ma on Line A, which is consistent with the previously proposed timing for the initiation of the Macquarie Plate (Cande and Stock, 2004a). Line B intersects the central part of segment KR1 (Fig. 1), where active hydrothermal venting sites have been reported (Hahm et al., 2015). Full-spreading rates estimated from Line B are relatively constant at 64∼66 mm/yr, similarly to Line A (Table S1). The geomagnetic polarities on Line B are symmetric and exhibit magnetic anomalies up to 3o (5.23 Ma) southward, and to 3Ay (6.04 Ma) northward (Fig. 2b). Line C was acquired along the western KR2 segment, and reveals geomagnetic anomalies up to 5o (10.95 Ma) for both its northern and southern flanks (Figs. 1 and 2c). For Line C, unlike Line A, no complicated crustal accretion history was required for forward modeling.

3. Revised Macquarie–Antarctic and Australian–Antarctic rotation parameters

3.1. Methodology

We computed finite rotation parameters for eight anomalies (1o, 2, 2Ay, 2Ao, 3y, 3o, 3Ay, and 3Ao) for the Macquarie–Antarctic motion using the newly acquired magnetic data, and the traces of fracture zones determined from the satellite-derived gravity grid (version 23) of Sandwell et al. (2014) (Fig. 3a). In addition, we employed archived magnetic data to expand the spatial and temporal coverage of our analysis, which are listed in the supplementary material. Although useful for filling gaps, we carefully assessed the quality of the archived data before conducting the subsequent analyses. Lastly, a set of short magnetic lines, collected in 2013 from the R/VIB *Araon*, were included in this study (red dashed lines with red shaded areas, perpendicular to the ridge in Fig. 3a). These data only extend to anomaly 1o (0.78 Ma).

The identified magnetic anomalies and fracture zone crossings were then utilized for computing finite rotation parameters for the Macquarie Plate relative to the Antarctic Plate using the Hellinger method (Hellinger, 1981; Kirkwood et al., 1999; Royer and Chang, 1991). We assigned a 1 km uncertainty to the locations of the new and well-navigated magnetic picks, and 4 km uncertainty to the picks that originated from the poorly navigated archives. Because the location of a FZ trace might be influenced by a long-term deformation integrated over several million years (Lonsdale, 1994), we assigned larger uncertainties to the FZ locations than for the magnetic picks (8 km for the long Balleny FZ and 5 km for the relatively short Tasman FZ; gray dashed lines in Fig. 3a).

Fig. 3 and Table 1 show the best-fit parameters and covariance matrices for the eight finite rotations describing the Macquarie–Antarctica motion. In this study, the second plate in all the considered plate pairs is held fixed, and hence used as the reference frame for each rotation. For example, the Antarctic Plate is fixed for the Macquarie–Antarctic motion. The solutions obtained from the

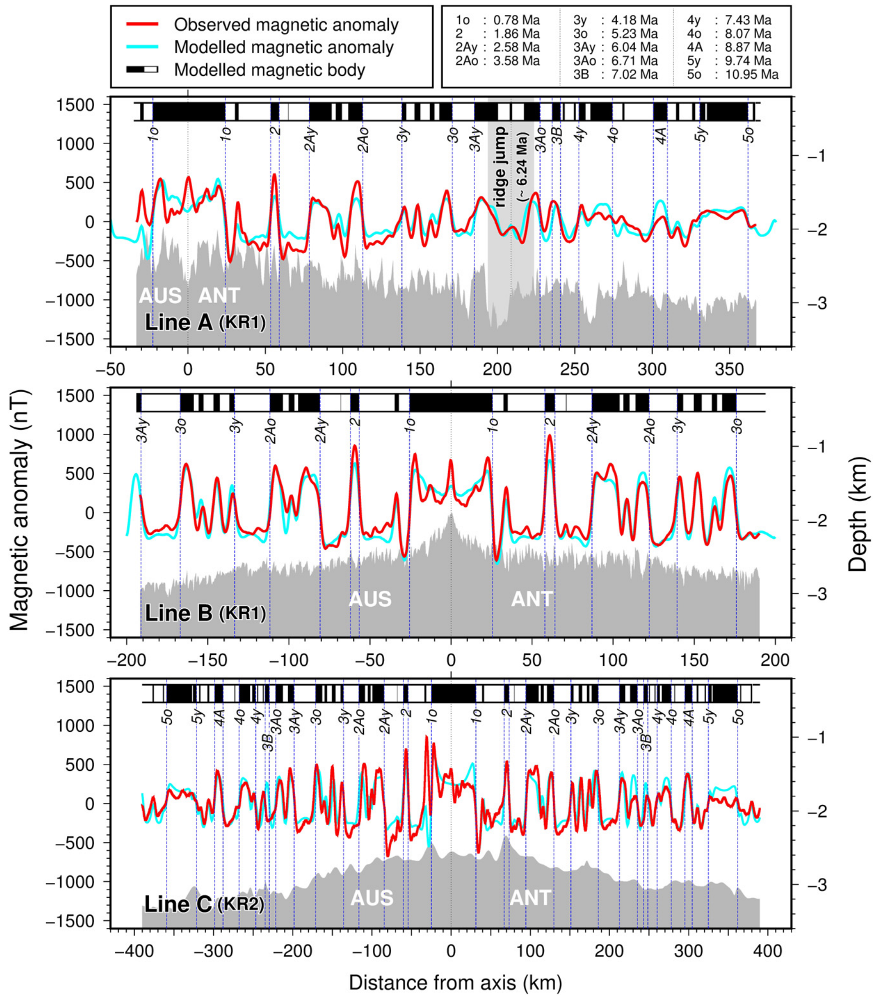

Fig. 2. Geomagnetic reversal models from the new shipboard magnetic data of Fig. 1. Red lines = observed magnetic anomalies; cyan lines = modeled magnetic anomalies. Black and white stripes show the normal and reverse magnetic intervals, respectively. All the geomagnetic polarity timescales used here are from Cande and Kent (1995), except for C3Ay and C3Ao, which are from Krijgsman et al. (1999). Gray-shaded areas represent shipboard (Lines A and B) and satellite-predicted bathymetry (Line C) (Smith and Sandwell, 1997). (For interpretation of the references to color in this figure legend, the reader is referred to the web version of this article.)

Hellinger method provide additional statistical information on the accuracy of the assigned errors for magnetic anomalies and fracture zones, denoted as $\hat{\kappa}$ (Chang, 1987, 1988). If $\hat{\kappa}$ is close to 1, then the assigned uncertainties are reasonably correct. For underestimated uncertainties, $\hat{\kappa}$ becomes $\ll 1$; for overestimated uncertainties, $\hat{\kappa}$ becomes $\gg 1$. For our data, the $\hat{\kappa}$ values are consistently larger than 1, indicating that the errors are overestimated. We performed the Hellinger computation using a range of assigned errors, and found that although the $\hat{\kappa}$ values vary (generally between 3 and 7), the resulting pole locations and the sizes of the uncertainty ellipses show only minor differences. Thus, we maintained the uncertainty assignments as described above for computing all the rotations.

For the finite rotation analyses, we follow Croon et al. (2008) and defined the magnetic anomalies of 3y and 3o as the polarity edges of chrons C3n.1n (m) (4.24 Ma) and C3n.4n (m) (5.11 Ma), respectively (where 'm' stands for the 'middle' of the normal polarity interval). This definition enabled us to combine our results with the Pacific–Antarctic rotations (Croon et al., 2008) and to calculate the Macquarie–Pacific relative plate motion.

3.2. Macquarie–Antarctic rotation parameters

Fig. 3a compares the location of our magnetic picks with their rotated conjugate picks. Using the new rotation parameters (Table 1), we find no distinct misfits between the rotated and non-rotated magnetic anomalies (average and maximum misfits are 0.30 and 2.50 km, respectively). In Fig. 3b, we display the new Macquarie–Antarctic finite rotation poles and their confidence ellipses, and compare them with the previous estimates (Cande and Stock, 2004a). Although the poles are spread in a NE–SW direction, their confidence ellipses overlap, meaning that these poles are indistinguishable from one another at the given 95% confidence level. This result further indicates that the direction of plate motion has been relatively consistent since the formation of the Macquarie Plate until the present. The confidence regions of the new Macquarie–Antarctic finite rotation poles overlap those of Cande and Stock (2004a) for anomalies 2Ay (2.58 Ma) and 3Ay (6.04 Ma) (Fig. 3b). The pole for the current motion between the plates (MORVEL, DeMets et al., 2010) is also located within the uncertainty ellipses of the poles of the new finite rotations (see letter 'M' in Fig. 3b).

3.3. Australian–Antarctic rotation parameters

Independently of the Macquarie Plate, we estimated the Australian–Antarctic plate motion using data straddling the central SEIR. The available archived magnetic data along the SEIR between the east Geelvinck FZ of 88°E and George V FZ of 140°E (Fig. 4a) obtained from the National Centers for Environmental Information (NCEI) were utilized (see the cruise list in the supplementary material) to calculate the Australian–Antarctic plate motion.

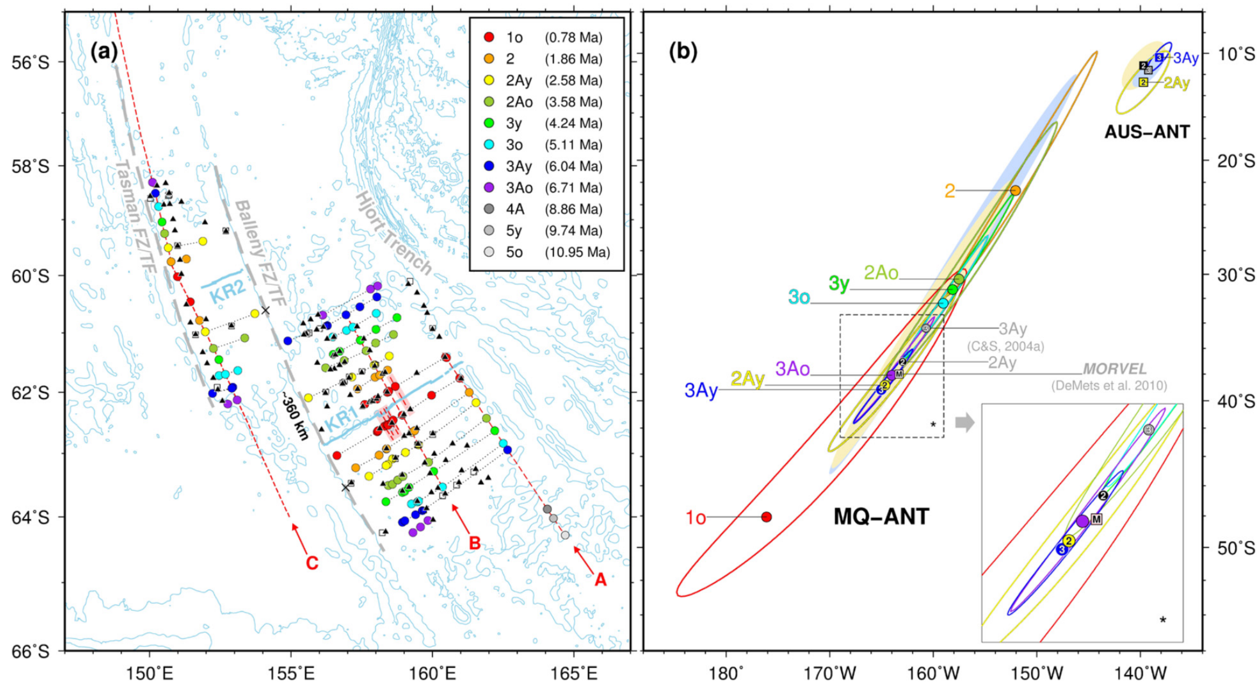

Fig. 3. (a) Magnetic anomaly locations, Balleny and Tasman Fracture Zones (FZs) utilized for estimating the Macquarie–Antarctic motion. Each magnetic pick is colored according to its corresponding polarity chron. Filled triangles are the rotated picks from the conjugate plate using our revised Macquarie–Antarctic rotation model (Table 1); the Antarctic Plate is fixed. Open squares are the rotated picks using the previous model (Cande and Stock, 2004a). The same isochrons (see x marks) of segments KR1 and KR2 are separated by ~360 km along the Balleny FZ and transform fault (TF). (b) New Macquarie–Antarctic finite rotation poles. The poles estimated in our study are shown by filled circles and solid lines. We display the C&S rotation poles (black (2Ay) and gray (3Ay) circles) (Cande and Stock, 2004a) and the MORVEL model (square with 'M') (DeMets et al., 2010). Shaded areas indicate the confidence regions of the previous study (Cande and Stock, 2004a; yellow for anomaly 2Ay, blue for 3Ay). The inset shows the areas (bounded by dotted lines) where the rotation poles are concentrated. (For interpretation of the references to color in this figure legend, the reader is referred to the web version of this article.)

Table 1
New finite rotations and covariance matrices for the Macquarie–Antarctic motion.[a]

Age[b] (Ma)	Magnetic anomaly	Polarity chron	Longitude (°E)	Latitude (°N)	Angle (degree)	Elements of covariance matrices[c] $\hat{\kappa}$	a	b	c	d	e	f	g	Mag. Pts	FZ Pts	Mag. Segs	FZ Segs
0.78	1o	C1n (o)	−176.101	−48.071	1.355	3.60	1.76	−0.80	3.21	0.37	−1.45	5.87	5	18	23	1	2
1.86	2	C2n (m)	−152.064	−22.734	1.386	16.1	1.83	−0.91	3.35	0.45	−1.65	6.15	5	14	27	2	2
2.58	2Ay	C2An.1n (y)	−164.680	−38.842	2.807	3.04	1.05	−0.54	1.92	0.28	−0.98	3.53	5	16	22	2	2
3.58	2Ao	C2An.3n (o)	−157.519	−30.398	3.101	1.76	1.38	−0.70	2.49	0.36	−1.26	4.53	5	14	28	2	2
4.24	3y	C3n.1n (m)	−158.138	−31.275	3.759	6.76	3.61	−1.72	6.42	0.82	−3.05	11.4	5	11	26	1	2
5.11	3o	C3n.4n (m)	−159.043	−32.401	4.680	5.15	2.31	−1.14	4.09	0.57	−2.01	7.28	5	13	28	2	2
6.04	3Ay	C3An.1n (y)	−165.016	−39.172	6.435	4.17	1.83	−0.92	3.20	0.47	−1.61	5.63	5	14	28	2	2
6.71	3Ao	C3An.2n (o)	−164.003	−38.083	6.937	4.22	3.57	−1.88	6.38	1.03	−3.41	11.5	5	9	28	2	2

[a] The Antarctic Plate is fixed.
[b] Ages are from Cande and Kent (1995), except for 3Ay and 3Ao, which are from Krijgsman et al. (1999).
[c] The covariance matrix as follows: $\frac{1}{\hat{\kappa}} * \begin{pmatrix} a & b & c \\ b & d & e \\ c & e & f \end{pmatrix} * 10^{-g}$.

As these magnetic data are not acquired within the diffuse deformation zones of the Capricorn–Australian (Cande and Stock, 2004a; Gordon et al., 2008; Royer and Gordon, 1997) and Australian–Macquarie plates (Cande and Stock, 2004a; DeMets et al., 2010; Hayes et al., 2009), the rotation parameters calculated using these identified picks presumably reflect the Australian–Antarctic plate motion.

Fig. 4 and Table 2 show the best-fit rotation parameters and covariance matrices for the Australian–Antarctic motion. Although we applied the same uncertainty assignment scheme to the magnetic anomalies and fracture zone picks described above, the $\hat{\kappa}$ values for the Australian–Antarctic rotations are mostly close to 1, indicating that the errors were correctly assigned. The lower $\hat{\kappa}$ values for the Australian–Antarctic rotations compared to those for the Macquarie–Antarctic rotations are mainly due to the increased number of relevant FZ segments. For the Macquarie–Antarctic motion, the Balleny and Tasman FZs are only the relevant FZ segments, and hence our estimates are inherently subject to larger $\hat{\kappa}$ values, leading to the larger uncertainty ellipses.

3.4. Rotation parameters of neighboring plates

Finally, we updated the finite rotation parameters of the Australian–Macquarie, Macquarie–Pacific, and Australian–Pacific motions using our new rotation parameters (Table 2). Because the Macquarie Plate interacts with the Pacific Plate across the Hjort Trench, using the Macquarie–Antarctic–Pacific plate circuit, we combined the Pacific–Antarctic rotations estimated by Croon et al. (2008) with our new Macquarie–Antarctic rotations to compute the Macquarie–Pacific relative plate motions. Fig. 5 shows the updated rotation poles and uncertainty ellipses. In general, compared to Cande and Stock (2004a), the confidence regions for anomalies 2Ay and 3Ay become much smaller and narrower.

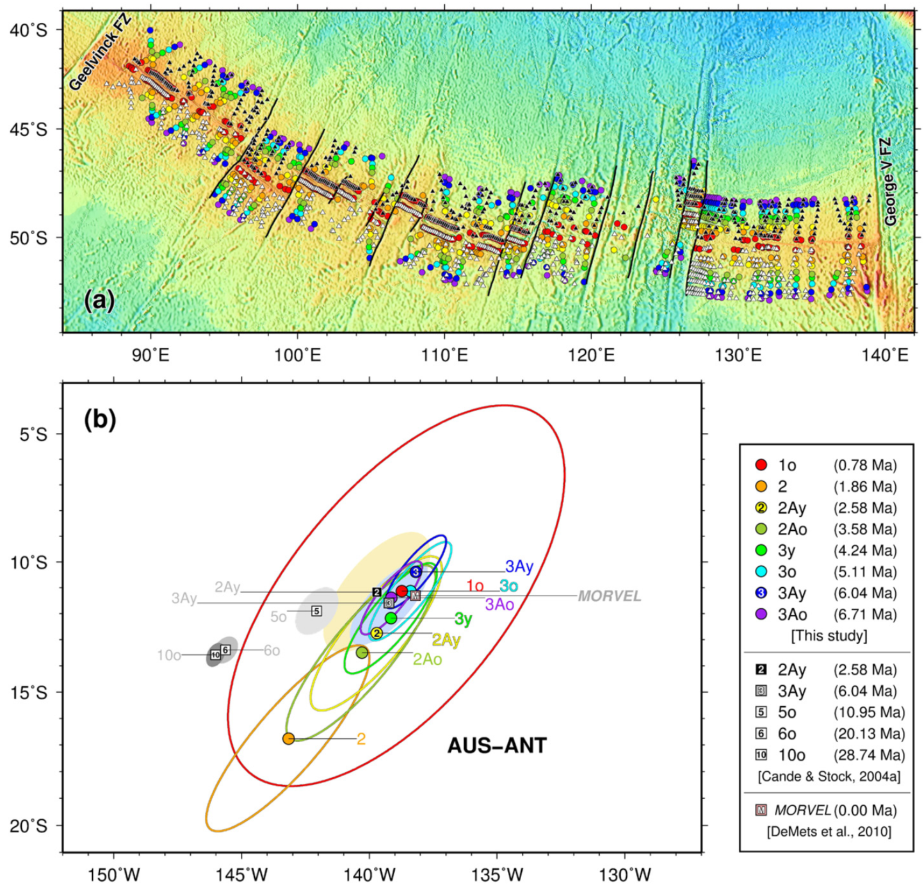

Fig. 4. (a) Magnetic anomaly locations (circles) and fracture zones (solid lines) used to estimate the Australia–Antarctic motion. The black and white triangles are the rotated picks from the Antarctic and Australian plates, respectively, using the new rotation poles (Table 2). The background grid is the satellite-derived seafloor topography (version 17) of Smith and Sandwell (1997). (b) New Australian–Antarctic finite rotation poles and corresponding 95% confidence regions with the fixed Antarctic Plate. We show the C&S rotation poles (squares) (Cande and Stock, 2004a) and the MORVEL model ('M') (DeMets et al., 2010). Shaded areas indicate the confidence regions of the C&S poles: yellow for anomaly 2Ay, blue for 3Ay, light-gray for 5o, medium-gray for 6o, and dark-gray for 10o. (For interpretation of the references to color in this figure legend, the reader is referred to the web version of this article.)

The most noticeable change among all the revised rotations is observed from the rotation poles of the Australian–Macquarie motion (Fig. 5a). In the previous work, the Australian–Macquarie rotations exhibited an apparent difference between the pole locations for 2Ay (2.58 Ma) and 3Ay (6.04 Ma) (Cande and Stock, 2004a). We find, however, that these poles are closely located to each other. In addition, the corresponding confidence regions are considerably better constrained, as compared with the previous estimates (see the color-shaded confidence areas (previous study) and those enclosed by yellow and blue solid lines (present study) in Fig. 5a).

Furthermore, our analyses exhibit a shortened distance between the Australian–Macquarie rotation poles of anomalies 2Ay and 3Ay, and place the new 3Ay southeast of the previous 3Ay (Cande and Stock, 2004a, Fig. 5a). Cande and Stock (2004a) suggested that moving the 3Ay pole farther east from the obtained best-fit location would be necessary to be consistent with the compressive deformation on the seafloor near 147∼148°E, 51∼52°S (see the black box in Fig. 6a). Such an adjustment of our result would resolve or reduce the mismatch between the predicted plate motion and the geophysical evidence for the existence of compressive structures.

4. Tectonic implications for the Macquarie Plate

The eastern boundary of the Macquarie Plate is well defined and runs along the Hjort Trench that extends south of the Macquarie Ridge (Fig. 6a). For the western boundary, we computed synthetic flowlines over several FZs using the Macquarie–Antarctic and Australian–Antarctic motions (Fig. 6a). The simulated flowlines from the Australian–Antarctic motion do not match with the Balleny and Tasman FZs (green solid lines in Fig. 6a), as previously noted in other studies (Cande and Stock, 2004a; Hayes et al., 2009), suggesting that the western boundary of the Macquarie Plate is located west of the Tasman FZ. Similarly, the simulated flowlines from the Macquarie–Antarctic motion do not match the St. Vincent and George V FZs, illustrating that the western end of the Macquarie Plate is located east of St. Vincent FZ.

The southern boundary of the Macquarie Plate was assigned to the KR1 and KR2 spreading segments, while the diffuse northern boundary has been poorly defined as the broad area between 50°S and 55°S, characterized by widespread intraplate earthquakes (Cande and Stock, 2004a). Using historical earthquakes since 1901 (from the U.S. Geological Survey) and the focal mechanisms since 1976 (from Global CMT solutions; Dziewonski et al., 1981), we estimate a diffuse zone between the Australian and Macquarie plates, extending between 50°S and 58°S, as the northern boundary of the Macquarie Plate (Fig. 6a).

Our finite rotation models indicate that the Macquarie Plate rotated clockwise with respect to the Australian Plate (Table 2). The rotation poles of the Australian–Macquarie motion are located within the diffused boundary zone between the two plates. The lithosphere west of the rotation poles, thus, inherently accommodates convergence (black arrow in Fig. 6a), whereas the lithosphere east of the poles accommodates divergence (white arrow in Fig. 6a) (e.g., Gordon et al., 2008; Royer and Gordon, 1997). In the conver-

Table 2
Revised finite rotations and covariance matrices near the Macquarie Plate.[a]

Age[b] (Ma)	Magnetic anomaly	Polarity chron	Longitude (°E)	Latitude (°N)	Angle (degree)	Elements of covariance matrices[c]								Mag. Pts	FZ Pts	Mag. Segs	FZ Segs
						$\hat{\kappa}$	a	b	c	d	e	f	g				
AUS–ANT																	
0.78	1o	C1n (o)	−138.732	−11.129	0.491	0.91	2.78	−4.08	1.85	10.0	−8.29	12.9	8	350	110	13	9
1.86	2	C2n (m)	−143.159	−16.761	1.204	1.57	0.68	−0.99	1.09	2.12	−2.27	3.21	7	117	157	10	9
2.58	2Ay	C2An.1n (y)	−139.706	−12.750	1.688	1.15	0.68	−0.97	1.01	2.11	−2.19	3.14	7	120	142	10	9
3.58	2Ao	C2An.3n (o)	−140.291	−13.495	2.347	0.50	0.70	−1.03	1.09	2.36	−2.44	3.37	7	99	150	7	9
4.24	3y	C3n.1n (m)	−139.153	−12.172	2.732	1.02	0.82	−1.15	1.22	2.49	−2.56	3.72	7	88	137	6	9
5.11	3o	C3n.4n (m)	−138.390	−11.127	3.275	0.94	0.92	−1.26	1.41	2.60	−2.76	3.92	7	86	139	7	9
6.04	3Ay	C3An.1n (y)	−138.179	−10.380	3.842	1.08	0.80	−1.11	1.17	2.32	−2.40	3.40	7	96	135	8	9
6.71	3Ao	C3An.2n (o)	−139.135	−11.386	4.287	0.92	0.87	−1.19	1.26	2.42	−2.51	3.58	7	93	129	8	9
AUS–MQ																	
0.78	1o	C1n (o)	154.560	−56.531	−1.092	0.96	1.77	−0.80	3.21	0.38	−1.45	5.88	5	N/A	N/A	N/A	N/A
1.86	2	C2n (m)	155.966	−39.255	−0.295	1.74	1.85	−0.91	3.37	0.47	−1.66	6.19	5	N/A	N/A	N/A	N/A
2.58	2Ay	C2An.1n (y)	150.094	−53.940	−1.700	1.25	1.07	−0.55	1.94	0.30	−1.00	3.56	5	N/A	N/A	N/A	N/A
3.58	2Ao	C2An.3n (o)	148.571	−49.559	−1.321	0.55	1.40	−0.71	2.52	0.38	−1.27	4.56	5	N/A	N/A	N/A	N/A
4.24	3y	C3n.1n (m)	149.982	−49.888	−1.766	1.16	3.67	−1.72	6.47	0.83	−3.03	11.5	5	N/A	N/A	N/A	N/A
5.11	3o	C3n.4n (m)	150.468	−50.291	−2.386	1.06	2.35	−1.14	4.13	0.57	−2.00	7.30	5	N/A	N/A	N/A	N/A
6.04	3Ay	C3An.1n (y)	148.095	−53.309	−4.110	1.21	1.88	−0.93	3.24	0.48	−1.61	5.64	5	N/A	N/A	N/A	N/A
6.71	3Ao	C3An.2n (o)	148.579	−52.856	−4.197	1.02	3.66	−1.88	6.45	1.02	−3.37	11.5	5	N/A	N/A	N/A	N/A
MQ–PAC																	
0.78	1o	C1n (o)	166.261	−58.775	1.888	3.56	1.76	−0.80	3.21	0.37	−1.45	5.87	5	N/A	N/A	N/A	N/A
1.86	2	C2n (m)	175.956	−57.809	2.343	11.5	1.84	−0.91	3.35	0.45	−1.65	6.15	5	N/A	N/A	N/A	N/A
2.58	2Ay	C2An.1n (y)	170.511	−58.497	4.415	2.99	1.06	−0.54	1.92	0.28	−0.98	3.53	5	N/A	N/A	N/A	N/A
3.58	2Ao	C2An.3n (o)	173.884	−58.106	5.156	1.74	1.38	−0.70	2.50	0.36	−1.26	4.53	5	N/A	N/A	N/A	N/A
4.24	3y	C3n.1n (m)	174.147	−58.130	6.251	6.40	3.62	−1.72	6.42	0.83	−3.05	11.5	5	N/A	N/A	N/A	N/A
5.11	3o	C3n.4n (m)	173.728	−58.102	7.736	5.00	2.31	−1.14	4.09	0.57	−2.01	7.28	5	N/A	N/A	N/A	N/A
6.04	3Ay	C3An.1n (y)	170.244	−58.697	10.268	4.11	1.83	−0.92	3.20	0.47	−1.61	5.64	5	N/A	N/A	N/A	N/A
6.71	3Ao	C3An.2n (o)	170.712	−58.586	11.163	3.95	3.57	−1.88	6.38	1.04	−3.41	11.5	5	N/A	N/A	N/A	N/A
AUS–PAC																	
0.78	1o	C1n (o)	−176.323	−59.760	0.814	0.91	2.90	−4.00	2.03	10.5	−7.50	13.3	8	N/A	N/A	N/A	N/A
1.86	2	C2n (m)	−179.640	−59.964	2.074	1.57	0.77	−0.99	1.17	2.19	−2.17	3.23	7	N/A	N/A	N/A	N/A
2.58	2Ay	C2An.1n (y)	−175.181	−59.123	2.776	1.15	0.95	−0.98	1.03	2.13	−2.16	3.23	7	N/A	N/A	N/A	N/A
3.58	2Ao	C2An.3n (o)	−175.394	−59.282	3.912	0.50	0.81	−1.02	1.22	2.44	−2.31	3.79	7	N/A	N/A	N/A	N/A
4.24	3y	C3n.1n (m)	−174.119	−59.399	4.582	1.03	0.93	−1.14	1.32	2.57	−2.45	4.06	7	N/A	N/A	N/A	N/A
5.11	3o	C3n.4n (m)	−173.526	−59.354	5.475	0.94	1.07	−1.25	1.62	2.67	−2.63	4.50	7	N/A	N/A	N/A	N/A
6.04	3Ay	C3An.1n (y)	−172.996	−58.955	6.342	1.09	1.19	−0.85	1.62	2.63	−2.02	4.19	7	N/A	N/A	N/A	N/A
6.71	3Ao	C3An.2n (o)	−173.923	−59.014	7.154	0.92	1.02	−1.17	1.50	2.49	−2.37	4.22	7	N/A	N/A	N/A	N/A

[a] The second plate in each pair is fixed (e.g., for MQ-PAC, the Pacific Plate is fixed).
[b] Ages are from Cande and Kent (1995), except for 3Ay and 3Ao, which are from Krijgsman et al. (1999).
[c] The covariance matrix as follows: $\frac{1}{\hat{\kappa}} * \begin{pmatrix} a & b & c \\ b & d & e \\ c & e & f \end{pmatrix} * 10^{-g}$.

gent region, as noted by Cande and Stock (2004a), our tectonic inference seems to be consistent with compressive deformation of the seafloor sediments imaged by single-channel seismic profiles on *Eltanin* cruise 53 (see the black box in Fig. 6a for the location). In the divergent region, Valenzuela and Wysession (1993) suggested that the lineations of broad gravity highs west of the Macquarie Ridge, which are consistent with the focal mechanisms near the Macquarie Ridge, could be indicative of extensional deformation of the crust. This coincides with the given sense of plate motion (white arrow in Fig. 6a).

Using the new finite rotation between the Australian and Macquarie plates, we reconstruct the relative motion between the plates in the diffuse zone from anomalies 3Ay and 2Ay to the present (Figs. 6b–c). The predicted motions between the Australian and Macquarie plates seem to show that the area west of the rotation pole in the diffuse zone, which includes the region obtained in the profile from *Eltanin* cruise 53, has been under a compressional regime (Fig. 6b), whereas extensional motion has been exerted, depending on the orientation of the feature that accommodated the motion, within the area east of the diffuse zone (Fig. 6c). Interestingly, the northeastern part of the diffuse zone was suggested to be connected with a propagating tear extending from southwest New Zealand (Hayes et al., 2009; Malservisi et al., 2003).

5. Kinematic evolution of the Macquarie Plate

In Fig. 7a, we predict the location of isochrons using the finite rotation model of the Macquarie–Antarctic plates for the last ∼10 Myr, by rotating the ridge axis of segment KR1 to the Antarctic Plate. The predicted isochrons are shown as black lines in Fig. 7a, whereas blue lines indicate the observed magnetic isochrons. For older isochrons (4A, 5y, and 5o), we extrapolated the rotation parameter of 3Ao to predict their locations (see red lines in Fig. 7a). Interestingly, this comparison between the predicted and observed magnetic isochrons reveals a sudden change in the spreading direction of segment KR1 between 4A (8.86 Ma) and 3Ay (6.04 Ma). Until ∼6 Ma the observed magnetic picks are closely approximated by the predicted isochrons, whereas the predicted locations for 4A, 5y, and 5o show large offsets from the observed locations. This primarily confirms that the Macquarie Plate was formed at ∼6 Ma, because the Macquarie–Antarctic plate motion is not adequate to predict the older isochrons. As the northward spreading prior to ∼6 Ma started to be obstructed by the subduction of young oceanic crust near the Hjort Trench (Cande and Stock, 2004a; Hayes et al., 2009), the seafloor spreading of segment KR1 might have been reorganized by rift propagation at ∼6.24 Ma, which was incorporated as a ridge-jump into the forward model (Table S1). In addition to the magnetic evidence from Line A (Fig. 2a), the high-resolution multi-beam and satellite-

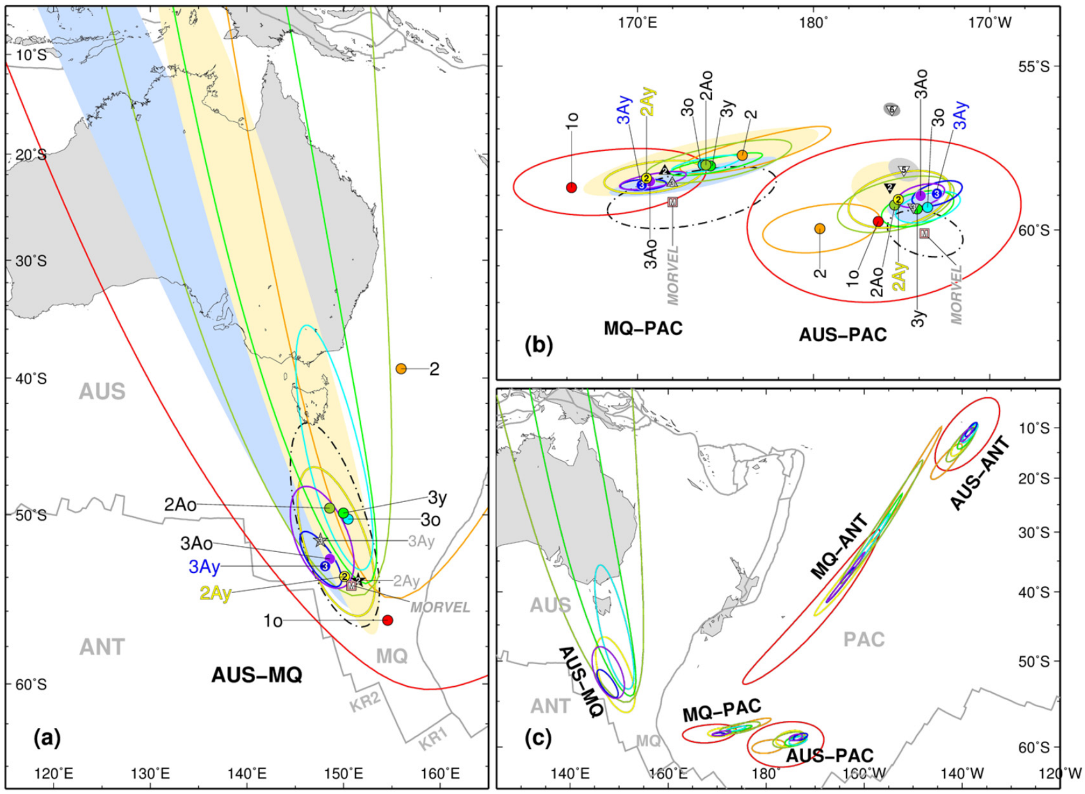

Fig. 5. (a) Revised rotation poles with corresponding 95% confidence ellipses for the Australian–Macquarie motion are compared with Cande and Stock (2004a) (black, gray stars, and shaded areas) and MORVEL ('M' and dotted line) (DeMets et al., 2010) models. Here the Macquarie Plate is fixed. (b) Revised rotation poles with 95% confidence ellipses for the Macquarie–Pacific and Australian–Pacific motions. For both motions, the Pacific Plate is fixed. (c) 95% confidence ellipses for all the revised rotation poles (red for anomaly 1o, 0.78 Ma; orange for 2, 1.86 Ma; yellow for 2Ay, 2.58 Ma; yellow-green for 2Ao, 3.58 Ma; green for 3y, 4.24 Ma; cyan for 3o, 5.11 Ma; blue for 3Ay, 6.04 Ma; purple for 3Ao, 6.71 Ma). For the Australian–Macquarie rotation, the ellipses for anomalies 1o and 2 are omitted to clarify the distinction among the rotation pairs because they are spread too wide. In all rotation pairs, the second plate is fixed (e.g., for AUS–ANT, the Antarctic Plate is fixed). (For interpretation of the references to color in this figure legend, the reader is referred to the web version of this article.)

derived free-air gravity data (see the inset in Fig. 7a) show a significant depression of the seafloor, bounded by steep cliffs. Such bathymetric variation may be directly associated with the corresponding rift propagation (Miller and Hey, 1986).

Rift propagation systems commonly develop a pair of pseudofaults between the young and older plates, creating age contrasts without actual relative motions between the plates (Hey, 2004; Matthews et al., 2016). Such well-developed pseudofaults are not found around the site of proposed rift propagator leading to ambiguity in its tectonic interpretation. One possible tectonic scenario that could explain these observations is a rapid propagation model (Fig. 7b). Based on the relationship between spreading rates and propagation rates expressed as $\alpha = \tan^{-1}(u/v)$ (Miller and Hey, 1986), the propagation rate (v) at the eastern KR1 segment is estimated to be faster than 100 mm/yr using the half-spreading rate (u) of ~32 mm/yr and half-angle of the propagation wedge (α) of ~15° measured from the bathymetric and gravity data (Fig. 7a). At intermediate- and fast-spreading ridges, if a ridge propagates at rates greater than ~50% of its corresponding full-spreading rate, then an asymmetric pseudofault can be formed as a linear trough (Matthews et al., 2016; Phipps Morgan and Sandwell, 1994). In this tectonic scenario, rapid rift propagation at ~6.24 Ma, which initiated from the MTJ or a fracture adjoining the northeastern KR1, produced the observed trough (Fig. 7b). In addition, the small age gap of ~0.2 Myr between the new rift and the pre-existing spreading center may explain the small negative gravity anomalies (Matthews et al., 2016; Phipps Morgan and Sandwell, 1994).

Alternatively, the observed ridge-jump (Fig. 2a) may be associated with an episodic migration of the MTJ. In Fig. 7c, we traced the roughly V-shaped seafloor lineations (dashed lines) from the vertical gravity gradient (VGG) data (version 23; Sandwell et al., 2014). If we consider the southern straight traces to be a linear outer pseudofault (OPF), then this OPF marks the WSW propagation of a new segment initiated near the MTJ prior to anomaly 5. Then, at anomaly 5, the propagation reversed as segment KR1 propagated to the ENE at the expense of the new segment, producing complex seafloor lineations that are apparent as an inner pseudofault (IPF). The traces of the IPF disappear at anomaly 3A, where the doubling of crust was found (yellow dashed line in Fig. 7c). In addition, another bathymetric low between anomalies 4y and 4o in Fig. 2a matches one of the IPF traces. This observation may indicate that MTJ migration contributed to the formation of the Macquarie Plate (e.g., Hey, 2004; Tebbens et al., 1997; Tebbens and Cande, 1997).

Unfortunately, the currently available data are not sufficient to either validate the proposed rapid propagation model (Fig. 7b) or to determine the interplay, if any, between the MTJ migration and formation of the Macquarie Plate (Fig. 7c). Finally, the changes in seafloor spreading direction and formation of the Macquarie Plate must have been predominantly accommodated by the Balleny and Tasman FZs, as no propagators are found near the central and western parts of the microplate. These unresolved tectonic problems, thus, should be studied in future works.

The detailed kinematic model of the Macquarie Plate since its formation until the present may provide new insights into the fragmentation of the oceanic lithosphere. One of the most relevant tectonic analog is that of microplate formation. For instance, Bird et al. (1998) presented the three-phase tectonic history of the Juan Fernandez (JF) Microplate. In response to a change in the Pacific–

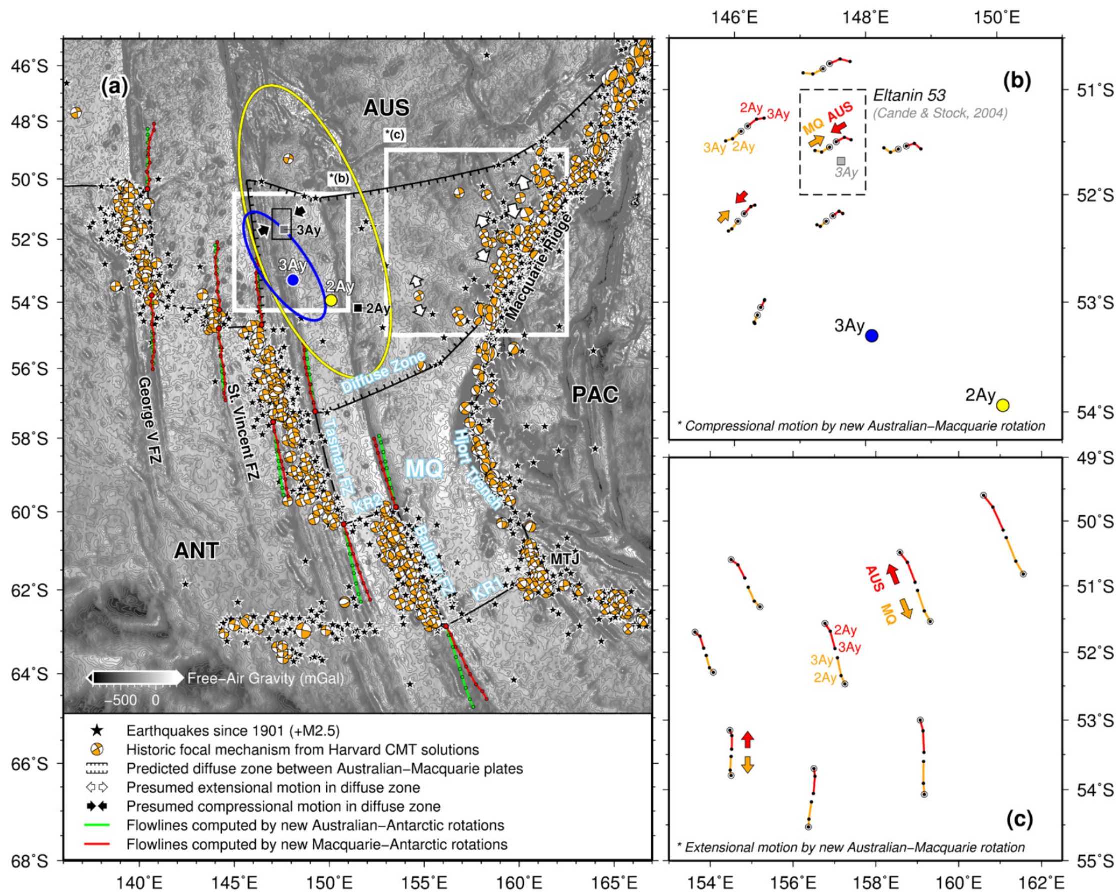

Fig. 6. (a) Macquarie Plate boundaries estimated from tectonic structure, intraplate earthquakes and synthetic flowlines calculated using the new Macquarie–Antarctic rotations are shown with light-blue-bordered white letters. The simulated flowlines by the new Macquarie–Antarctic motion (red lines) show good agreement with the Balleny and Tasman FZs only, whereas the simulated flowlines by the new Australian–Antarctic motion (green lines) are relatively consistent with the FZs west of Tasman FZ. The revised rotation poles and 95% confidence regions for the Australian–Macquarie motion are shown by yellow (2Ay) and blue (3Ay) colors (circles for poles, and solid lines for ellipses). In order to simplify the map, the new rotation poles and confidence regions of the remaining anomalies are omitted; specifically, 1o, 2, 2Ao, and 3y are too wide to be displayed in the given map domain. Black (2Ay) and gray (3Ay) squares are the previous rotation poles (Cande and Stock, 2004a). Earthquakes >2.5 (+M2.5) since 1901 (black stars) (from U.S. Geological Survey) and the focal mechanism since 1976 (from Global CMT solutions; Dziewonski et al., 1981) are shown on the map. The motions in the diffuse boundary zone between the Australian–Macquarie plates (black and white arrows) are estimated using the new Australian–Macquarie motion. (b) Compressional motions at the western portion of the diffuse zone, calculated using the new Australian–Macquarie rotations from the anomalies 3Ay and 2Ay to present. The dashed box is the area denoted with the black box in (a), where compressive deformation of seafloor sediments was imaged by *Eltanin* cruise 53 (Cande and Stock, 2004a). (c) Extensional motions at the eastern portion of the diffuse zone, calculated using the new Australian–Macquarie rotations from the anomalies 3Ay and 2Ay to present. (For interpretation of the references to color in this figure legend, the reader is referred to the web version of this article.)

Nazca spreading direction, the JF Microplate formed and grew by rapidly propagating rifts, exhibiting slow microplate rotation during phase 1 (∼6.0–2.6 Ma) (Bird et al., 1998). Subsequently, the microplate rotation increased by a factor of three with a series of plate boundary reorganizations during phase 2 (2.6–1.1 Ma), and decreased to the current rate due to increased coupling between the JF Microplate and the Antarctic Plate during phase 3 (1.1 Ma to present). Interestingly, a similar pattern, involving a rapid increase in spreading rates followed by a long decay, has been observed in several incipient oceanic basins (e.g., Brune et al., 2016; Granot and Dyment, 2015) and was attributed to the nonlinear decay of the resistive rift strength force (Brune et al., 2016). The Macquarie Plate appears to have undergone similar stages of kinematic evolution. We converted the finite rotation models estimated in this study (Tables 1 and 2) to corresponding stage poles and angular velocities with uncertainties (Fig. 8) using the *rotconverter* program in GMT (Wessel et al., 2013) and Hellinger's *addrot* program (Kirkwood et al., 1999), respectively. For the Macquarie–Antarctic rotation (Fig. 8a), the angular velocity of the Macquarie Plate relative to the fixed Antarctic Plate increased by ∼2.5 times between anomaly 3Ay (6.04 Ma) and anomaly 3y (4.24 Ma) compared to the rates prior to anomaly 3Ay (6.04 Ma), after the reorganization of the spreading direction at segment KR1 was completed at ∼6.24 Ma.

Since the formation of the Macquarie Plate, no distinct change in the Macquarie–Antarctic spreading direction has been observed (Fig. 3b), and hence no further reorganization is needed. As the rate of the JF Microplate rotation decreased to its present rate during the last phase, the Macquarie Plate also exhibits a similar systematic reduction in angular velocity ($<1°$/Myr) of the Macquarie Plate relative to the Antarctic Plate after another abrupt increase between anomalies 2Ay (2.58 Ma) and 2 (1.86 Ma) (Fig. 8a). In addition, such temporal changes in the Macquarie–Antarctic angular velocity are only apparent in the motions of immediately neighboring plates (Figs. 8b–c), whereas the angular velocities between the other large plates have been relatively stable, with no significant changes during and after the generation of the Macquarie Plate (Figs. 8a–b).

It is notable that the Macquarie Plate has been growing at a constant rate by seafloor spreading (see spreading rates in Table S1), whereas the Macquarie-related rotation exhibits temporal variations (Figs. 8b-c). Besides the possible decrease in the resistive strength force, variations in slab-pull forces along the Hjort Trench may have contributed to the increase in angular velocity. As

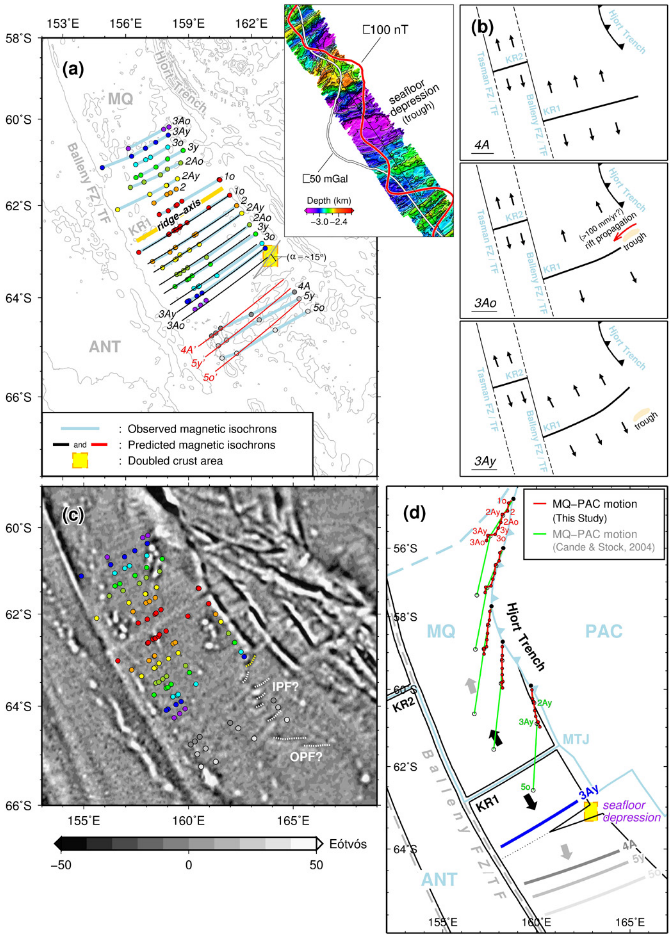

Fig. 7. (a) Comparison between the observed and predicted magnetic isochrons along segment KR1. Blue lines show the observed magnetic isochrons, whereas red and black lines indicate the rotated positions of the KR1 ridge axis using the half-angle of each rotation. For anomalies 4A (8.86 Ma), 5y (9.74 Ma), and 5o (10.95 Ma), the angular velocity of anomaly 3Ao was used to extrapolate the finite rotation angle for each case. While the rotated axes closely approximate the observed isochrons for the last ∼6 Myr, misfits between the predicted and observed isochrons become apparent beyond anomaly 3Ay (6.04 Ma). This demonstrates that segment KR1 has reorganized the spreading direction with a small ridge-jump accompanying seafloor depression, which was observed from the shipboard magnetics, bathymetry, and satellite-derived free-air gravity (see the inset). (b) Schematic diagrams illustrating the tectonic reorganization processes with a rapid rift propagation near KR1. If the observed ridge-jump is associated with the proposed rapid propagation model, a trough next to the rift propagation would be produced instead of a pair of pseudofaults (Matthews et al., 2016; Phipps Morgan and Sandwell, 1994). The half-angle of the propagation wedge (α) is shown in (a). (c) Seafloor lineations (dashed lines) mapped using the vertical gravity gradient (VGG) data (version 23; Sandwell et al., 2014). The color-coded circles are the estimated magnetic picks. The southern straight traces are considered as a linear outer pseudofault (OPF), whereas other northern lineations are marked as an inner pseudofault (IPF). This may indicate episodic migration of the MTJ. The area displaying doubling of the crust is denoted by a yellow dashed line. (d) Schematic map showing the kinematic behavior of the Macquarie Plate. The revised Macquarie–Pacific motion (red solid lines) shows the spatial and temporal variations of the Macquarie Plate motion along the Hjort Trench since its formation. The previous study (Cande and Stock, 2004a) was unable to resolve such details due to lack of shipboard magnetics (green solid lines). (For interpretation of the references to color in this figure legend, the reader is referred to the web version of this article.)

such, the ridge-push from the southern boundary at intermediate spreading rates may not have been sufficient to induce large-scale lithospheric deformation by compression in the west and extension in the east of the diffuse boundary area (Fig. 6). Meckel et al. (2003) showed that the northern and central Hjort Trench, characterized by low-angle oblique-slip faults, is more evolved than the southern part of the trench, which may represent incipient subduction of the Macquarie Plate. Such spatial changes in subduction along the Hjort Trench appear to be consistent with the clockwise Macquarie–Pacific plate rotation. If such slab-pull effects existed, they could be another factor affecting the angular velocities of the Macquarie–Pacific rotation. The newly estimated Macquarie–Pacific motion shows the motions of the Macquarie Plate relative to the Pacific Plate are more toward the Pacific Plate along the northern Hjort Trench than along the southern part of the trench (see red lines in Fig. 7d). These Pacific-ward motions may be an indicative of such slab-full effects.

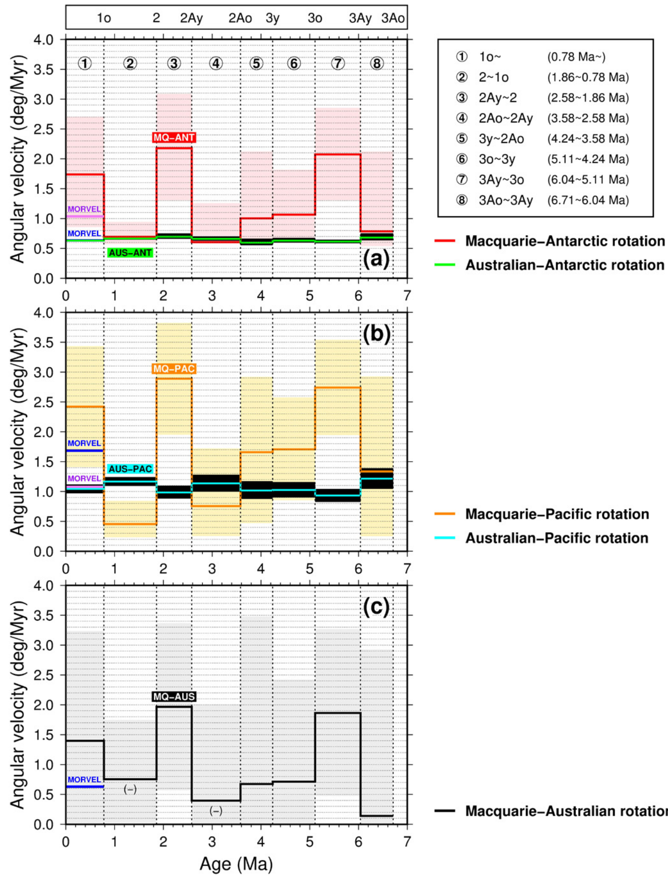

Fig. 8. Plate rotation velocities and uncertainty ranges for (a) Macquarie–Antarctic (red lines and light red areas) and Australian–Antarctic (green lines and black areas) motions, and (b) Macquarie–Pacific (orange lines and yellow areas) and Australian–Pacific (cyan lines and black areas) motions, and (c) Macquarie–Australian (black lines and gray areas) motion. All the Macquarie-associated motions display a rapid increase in angular velocity at ∼6 Ma, whereas the Australian–Pacific and Australian–Antarctic plates exhibit no distinct changes in motion or velocity. All the newly estimated angular velocities are compared with the MORVEL (0.78 Ma∼) results of DeMets et al. (2010). For the Macquarie–Australian motion, the rotation direction becomes negative (i.e., counter-clockwise rotation) during stages 2 and 4. The corresponding stage poles and their confidence regions are displayed in Fig. S1. In all the considered motions, the second plate is fixed. For the case of the Macquarie–Australian rotation, however, the negative angular velocities (marked with a minus sign) are plotted on the positive domain for graphical purposes only. (For interpretation of the references to color in this figure legend, the reader is referred to the web version of this article.)

In addition, previous studies suggested that the changes of the relative plate motion and absolute plate motion across the circum-Pacific rim have occurred at ∼6 Ma, ∼2.6 Ma, and ∼0.78 Ma (Cande et al., 1995; Wessel and Kroenke, 2000); interestingly, these timings coincide with the temporal variation in the angular velocity of Macquarie-involved plate motions (Fig. 8).

Among the main triggers of microplate formation including plate reorganization, triple junction migration, plume activity, and fast spreading (Hey, 2004; Matthews et al., 2016), the first two processes appear to be most relevant with the kinematic evolution of the Macquarie Plate. According to previous studies, around C3A (∼6 Ma) the SEIR appeared to undergo a clockwise change in spreading direction of 20°, with an increase in spreading rate (Cande and Kent, 1992). At the same time, there was another clockwise change in spreading direction of the Pacific–Antarctic Ridge (Austermann et al., 2011; Cande et al., 1995; Cande and Stock, 2004b; Croon et al., 2008; Lodolo and Coren, 1997; Wessel and Kroenke, 2000). At the Pacific–Nazca boundary, a change in spreading direction at ∼6 Ma caused the formation of microplates, such as the Easter (Bird and Naar, 1994; Naar and Hey, 1991; Neves et al., 2003; Rusby and Searle, 1995) and Juan Fernandez (JF) microplates (Bird et al., 1998; Bird and Naar, 1994; Searle et al., 1993). The formation of the JF Microplate was triggered by a change in the Pacific–Nazca spreading direction of ∼5°. Similarly, a ∼10° change in the Australian–Antarctic spreading direction, as estimated from segment KR1, appears to have initiated the generation of the Macquarie Plate. In addition, the relationship between MTJ migration and formation of the Macquarie Plate needs to be evaluated with better data coverage.

6. Conclusions

We analyzed new shipboard magnetic data collected at segments KR1 and KR2 of the easternmost Southeast Indian Ridge (SEIR). For eight anomalies (1o, 2, 2Ay, 2Ao, 3y, 3o, 3Ay, and 3Ao), we determined finite rotation parameters for the Macquarie–Antarctic and Australian–Antarctic plate pairs using archived and newly acquired magnetic anomalies. We then summed these rotation parameters to revise the Australian–Macquarie, Macquarie–Pacific, and Australian–Pacific motions. Compared to previous analyses, the updated rotation poles exhibit more tightly located poles for anomalies 2Ay and 3Ay, with significantly smaller and narrower confidence regions.

The change in Australian–Antarctic spreading direction from N–S to NW–SE appears to initiate the formation of the Macquarie Plate at ∼6.24 Ma. The stage poles estimated from the new finite rotations exhibit the temporal change of angular velocity for the Macquarie–related motions, which may indicate that the resisting force of young oceanic crust against subduction at the Hjort Trench sustained only the initial development stage of the Macquarie Plate. During the growth stage, we speculate that the independent motion of the Macquarie Plate was enhanced by the increased subducting rates at the Hjort Trench and the decrease in the resistive strength, while the Macquarie Plate has exhibited constant growth by seafloor spreading.

The Macquarie Plate has a unique tectonic setting, consisting of two spreading axes to the south, a diffuse boundary to the north, and subduction and transform faults in the other two sides of the plate. This may have resulted in the differential development processes of the new plate boundaries of the Macquarie Plate, as compared with other oceanic microplates.

Acknowledgements

We thank the captains and crews of the R/VIB *Araon* and M/V *L'Astrolabe* for their efforts during the cruises. This study was supported by PE17050, funded by the Korea Polar Research Institute. SSK acknowledges support from the National Research Foundation (NRF) grant NRF-2013R1A1A1076071 funded by the Ministry of Science, ICT and Future Planning, and grant NRF-2017R1D1A1A02018632 funded by the Ministry of Education, Korea. We thank the editor Peter Shearer and two anonymous reviewers for their thorough and constructive comments that improved the manuscript greatly.

Appendix A. Supplementary material

Supplementary material related to this article can be found online at http://dx.doi.org/10.1016/j.epsl.2017.08.035.

References

Austermann, J., Ben-Avraham, Z., Bird, P., Heidbach, O., Schubert, G., Stock, J.M., 2011. Quantifying the forces needed for the rapid change of Pacific plate motion at 6 Ma. Earth Planet. Sci. Lett. 307, 289–297.
Bird, R.T., Naar, D.F., 1994. Intratransform origins of mid-ocean ridge microplate. Geology 22, 987–990.
Bird, R.T., Naar, D.F., Larson, R.L., Searle, R.C., Scotese, C.R., 1998. Plate tectonic reconstructions of the Juan Fernandez microplate: transformation from internal shear to rigid rotation. J. Geophys. Res. 103, 7049–7067.
Brune, S., Williams, S.E., Butterworth, N.P., Müller, R.D., 2016. Abrupt plate accelerations shape rifted continental margins. Nature 536, 201–204.
Cande, S.C., Kent, D.V., 1992. A new geomagnetic polarity time scale for the Late Cretaceous and Cenozoic. J. Geophys. Res. 97, 13917–13951.
Cande, S.C., Kent, D.V., 1995. Revised calibration of the geomagnetic polarity timescale for the Late Cretaceous and Cenozoic. J. Geophys. Res. 100, 6093–6095.
Cande, S.C., Raymond, C.A., Stock, J., Haxby, W.F., 1995. Geophysics of the Pitman Fracture Zone and Pacific–Antarctic plate motions during the Cenozoic. Science 270, 947–953.
Cande, S.C., Stock, J.M., 2004a. Pacific–Antarctic–Australia motion and the formation of the Macquarie Plate. Geophys. J. Int. 157, 399–414.
Cande, S.C., Stock, J.M., 2004b. Cenozoic reconstruction of the Australia–New Zealand–South Pacific sector of Antarctica. In: Exon, N.F., Kennett, J.K., Malone, M.J. (Eds.), The Cenozoic Southern Ocean: Tectonics, Sedimentation and Climate Change Between Australia and Antarctica. AGU, Washington DC, pp. 5–15.
Chang, T., 1987. On the statistical properties of estimated rotations. J. Geophys. Res. 92, 6319–6329.
Chang, T., 1988. Estimating the relative rotation of two tectonic plates from boundary crossings. J. Am. Stat. Assoc. 83, 1178–1183.
Croon, M.B., Cande, S.C., Stock, J.M., 2008. Revised Pacific–Antarctic plate motions and geophysics of the Menard Fracture Zone. Geochem. Geophys. Geosyst. 9, Q07001.
Crowley, J.W., Katz, R.F., Huybers, P., Langmuir, C.H., Park, S.-H., 2015. Glacial cycles drive variations in the production of oceanic crust. Science 347, 1237–1240.
DeMets, C., Gordon, R.G., Argus, D.F., 1988. Intraplate deformation and closure of the Australia–Antarctica–Africa plate circuit. J. Geophys. Res. 93, 11877–11897.
DeMets, C., Gordon, R.G., Argus, D.F., 2010. Geologically current plate motions. Geophys. J. Int. 181, 1–80.
Dziewonski, A.M., Chou, T.-A., Woodhouse, J.H., 1981. Determination of earthquake source parameters from waveform data for studies of global and regional seismicity. J. Geophys. Res. 86, 2825–2852.
Gordon, R.G., Argus, D.F., Royer, J.-Y., 2008. Space geodetic test of kinematic models for the Indo-Australian composite plate. Geology 36, 827–830.
Granot, R., Dyment, J., 2015. The Cretaceous opening of the South Atlantic Ocean. Earth Planet. Sci. Lett. 414, 156–163.
Hahm, D., Baker, E.T., Rhee, T.S., Won, Y.-J., Resing, J.A., Lupton, J.E., Lee, W.-K., Kim, M., Park, S.-H., 2015. First hydrothermal discoveries on the Australian–Antarctic Ridge: discharge sites, plume chemistry, and vent organisms. Geochem. Geophys. Geosyst. 16, 3061–3075.
Hayes, G.P., Furlong, K.P., Ammon, C.J., 2009. Intraplate deformation adjacent to the Macquarie Ridge south of New Zealand — the tectonic evolution of a complex plate boundary. Tectonophysics 463, 1–14.
Hellinger, S.J., 1981. The uncertainties of finite rotations in plate tectonics. J. Geophys. Res. 86, 9312–9318.
Hey, R.N., 2004. Propagating rifts and microplates at mid-ocean ridges. In: Selley, R.C., et al. (Eds.), Encyclopedia of Geology. Academic Press, London, pp. 396–405.
Kirkwood, B.H., Royer, J.-Y., Chang, T.C., Gordon, R.G., 1999. Statistical tools for estimating and combining finite rotations and their uncertainties. Geophys. J. Int. 137, 408–428.
Krijgsman, W., Hilgen, F.J., Raffi, I., Sierro, F.J., Wilson, D.S., 1999. Chronology, causes and progression of the Messinian salinity crisis. Nature 400, 652–655.
Lodolo, E., Coren, F., 1997. A Late Miocene plate boundary reorganization along the westernmost Pacific–Antarctic ridge. Tectonophysics 274, 295–305.
Lonsdale, P., 1994. Structural geomorphology of the Eltanin fault system and adjacent transform faults of the Pacific–Antarctic plate boundary. Mar. Geophys. Res. 16, 105–143.
Malservisi, R., Furlong, K.P., Anderson, H., 2003. Dynamic uplift in a transpressional regime: numerical model of the subduction area of Fiordland, New Zealand. Earth Planet. Sci. Lett. 206, 349–364.
Matthews, K.J., Müller, R.D., Sandwell, D.T., 2016. Oceanic microplate formation records the onset of India–Eurasia collision. Earth Planet. Sci. Lett. 433, 204–214.
Meckel, T.A., Coffin, M.F., Mosher, S., Symonds, P., Bernardel, G., Mann, P., 2003. Underthrusting at the Hjort Trench, Australian–Pacific plate boundary: incipient subduction? Geochem. Geophys. Geosyst. 4, 1099.

Mendel, V., Munschy, M., Sauter, D., 2005. MODMAG, a MATLAB program to model marine magnetic anomalies. Comput. Geosci. 31, 589–597.
Miller, S.P., Hey, R.N., 1986. Three-dimensional magnetic modeling of a propagating rift, Galapagos 95°30′W. J. Geophys. Res. 91, 3395–3406.
Naar, D.F., Hey, R.N., 1991. Tectonic evolution of the Easter microplate. J. Geophys. Res. 96, 7961–7993.
Neves, M.C., Searle, R.C., Bott, M.H.P., 2003. Easter microplate dynamics. J. Geophys. Res. 108, 2213.
Phipps Morgan, J., Sandwell, D.T., 1994. Systematics of ridge propagation south of 30°S. Earth Planet. Sci. Lett. 121, 245–258.
Royer, J.-Y., Chang, T., 1991. Evidence for relative motions between the Indian and Australian plates during the last 20 m.y. from plate tectonic reconstructions: implications for the deformation of the Indo–Australian Plate. J. Geophys. Res. 96, 11779–11802.
Royer, J.-Y., Gordon, R.G., 1997. The motion and boundary between the Capricorn and Australian plates. Science 277, 1268–1274.
Rusby, R.I., Searle, R.C., 1995. A history of the Easter microplate, 5.25 Ma to present. J. Geophys. Res. 100, 12617–12640.
Sandwell, D.T., Müller, D.R., Smith, W.H.F., Garcia, E., Francis, R., 2014. New global marine gravity model from CryoSat-2 and Jason-1 reveals buried tectonic structure. Science 346, 65–67.
Searle, R.C., Bird, R.T., Rusby, R.I., Naar, D.F., 1993. The development of two oceanic microplates: Easter and Juan Fernandez microplates, East Pacific Rise. J. Geol. Soc. Lond. 150, 965–976.
Seton, M., Whittaker, J.M., Müller, R.D., DeMets, C., Merkouriev, S., Cande, S.C., Gaina, C., Eagles, G., Granot, R., Stock, J., Wright, N., Williams, S., 2014. Community infrastructure and repository for marine magnetic identifications. Geochem. Geophys. Geosyst. 15, 1629–1641.
Smith, W.H.F., Sandwell, D.T., 1997. Global seafloor topography from satellite altimetry and ship depth soundings. Science 277, 1957–1962.
Tebbens, S.F., Cande, S.C., Kovacs, L., Parra, J.C., LaBrecque, J.L., Vergara, H., 1997. The Chile ridge: a tectonic framework. J. Geophys. Res. 102, 12035–12059.
Tebbens, S.F., Cande, S.C., 1997. Southeast Pacific tectonic evolution from Early Oligocene to present. J. Geophys. Res. 102, 12061–12084.
Thébault, E., Finlay, C., Beggan, C., Alken, P., Aubert, J., Barrois, O., Bertrand, F., Bondar, T., Boness, A., Brocco, L., Canet, E., Chambodut, A., Chulliat, A., Coisson, P., Civet, F., Du, A., Fournier, A., Fratter, I., Gillet, N., Hamilton, B., Hamoudi, M., Hulot, G., Jager, T., Korte, M., Kuang, W., Lalanne, X., Langlais, B., Leger, J.-M., Lesur, V., Lowes, F., 2015. International geomagnetic reference field: the 12th generation. Earth Planets Space 67, 79.
Valenzuela, R.W., Wysession, M.E., 1993. Intraplate earthquakes in the southwest Pacific Ocean basin and the seismotectonics of the southern Tasman Sea. Geophys. Res. Lett. 20, 2467–2470.
Wessel, P., Kroenke, L.W., 2000. Ontong Java Plateau and late Neogene changes in Pacific Plate. J. Geophys. Res. 105, 28255–28277.
Wessel, P., Smith, W.H.F., Scharroo, R., Luis, J.F., Wobbe, F., 2013. Generic mapping tools: improved version released. Eos 94, 409–410.